ELSEVIER

Computational fluid dynamics simulations yielding guidelines for the ideal internal structure of monolithic liquid chromatography columns[☆]

P. Gzil*, G.V. Baron, G. Desmet

Vrije Universiteit Brussel, Department of Chemical Engineering, Pleinlaan 2, 1050 Brussels, Belgium

Abstract

A theoretical calculation of the separation performance of a (hypothetical) micro-structured monolithic LC column is presented, confirming that the polydispersity effect in parallel bundle columns can theoretically be eliminated to a very large extent by radially redistributing the mobile phase fluid at regular intervals. It is demonstrated that the flow can be redistributed in such a way that the advantage coming from the suppression of the polydispersity effect largely exceeds the losses caused by the additional pressure-drop and band broadening. The presently considered micro-structured column would allow to perform $N > 100\,000$ plate separations in a few hundred of seconds, i.e., about an order of magnitude faster than the best possible packed bed and monolithic HPLC columns, while offering the same mass loadability. This clearly demonstrates that the currently available LC columns are still far away from the absolute resolution limit of the ideal, fully optimised LC column.
© 2003 Published by Elsevier Science B.V.

1. Introduction

With the demand for increased separation capacity coming from applications such as proteomics research and drug screening, the field of analytical chemistry is currently under pressure to find a method to perform separations yielding >100 000 plates in a sufficiently short time [1]. With packed bed high-performance liquid chromatography (HPLC), the analysis times are too large, and a reduction of the analysis time can only be obtained by applying extremely large inlet pressures, such as is done in ultra-high-pressure LC (UHP-LC [2,3]). The currently most successful approach to yield $N > 10\,000$ plates is based on switching from a pressure-driven to an electrically-driven mode for the propulsion of the mobile phase fluid [4,5]. The numerous reports [6–8] on the performance of capillary electrochromatography (CEC) clearly show that efficiencies of up to 150 000 plates per column can be reached with this approach [1]. The field

however still struggles with difficult problems such as frit reproducibility, the dependency of the flow-rate on slight changes of the fluid composition and viscosity, and on the adsorption of macro-molecular impurities or sample components on the column wall or the packing [8,9].

In the present study, we look at the improvements which can be expected from a change in the column architecture rather than from a change of the flow-driving method. This interest is inspired by the recent reports [10–14] on the superior performance of monolithic columns and their commercial success (cf. Merck's Chromolith column). This success has made clear that there is sufficient reason to question the position of the traditional packed bed of spheres as the ideal LC column format. In fact, it is as long ago as the late 1970s [15] that the shortcomings of the packed bed (large eddy-dispersion and large flow resistance) were recognized and that the advantages of open-tubular LC (OT-LC), with its per definition straight, unobstructed flow path, were pursued. Despite of its intrinsic theoretical superiority, the OT-LC concept has however never gained great popularity. As has been abundantly demonstrated by Poppe [16] and many others [17,18], this lack of success can be entirely blamed on the poor mass loadability and retention power of such columns.

One of the obvious solutions to get round the poor mass loadability of the OT-LC column format would be to multiply the number of flow channels and to consider a bundle of parallel open-tubular columns. In this concept, the tortuous path through the packed bed is replaced by a parallel array of unobstructed flow paths, retaining the ideal combination of minimal flow resistance and minimal plate height of OT-LC, while the overall mass loadability can be kept at the same level of a conventional packed wide-bore column, simply by arraying a sufficient number of capillary columns. The experimental exploration of the concept however only yielded disappointing results [19], because, as has been demonstrated very elegantly by Schisla et al. [20], the inevitable channel-to-channel diameter variability (or polydispersity) creates a fundamental source of additional band broadening which completely deteriorates the quality of the separations. They showed that even a polydispersity of only 1% can increase the theoretical plate height by as much as an order of

magnitude. As suggested by the authors of the same study, the only possible way to reduce this polydispersity effect would be to cut the bundle of capillaries into several segments, rotate the individual segments around their longitudinal axis over a random angle and then reconnect them. In this way, a stochastic redistribution of the flow is obtained at regular intervals, creating the radial mixing needed to even out the inevitable differences in flow velocity among the different individual capillaries. The idea has however always remained a purely theoretical thought, partly because the "gluing" of the different segments seems practically impossible, especially when considering the large sealing problems. The authors were also concerned that the introduction of many coupling sections would resurrect the pressure drop problem [20]. It has also never been calculated what the ideal length of the individual segments should be, i.e., it is up to now not very clear whether the segments would have a manageable length or not, and there is no theoretical framework to produce a good estimate for it. Finding the optimal segment length is not trivial, because packing structures with longer, parallel running channels have a smaller flow resistance on the one hand, but, since the number of opportunities for radial mixing is much smaller, such columns are much more prone to the polydispersity effect. By increasing the number of segments, the flow channel interconnectivity increases, hence reducing the polydispersity effect, but on the other hand, as each connection segment constitutes an additional pressure drop and axial dispersion source, the overall flow resistance and plate height value of the column increases as well. It is hence obvious to expect that the optimal column design will be reached at some intermediate degree of segmentation (Fig. 1).

In the present paper, a very simple segmented column design is considered (Fig. 2), offering a potential solution for the segment connection prob-
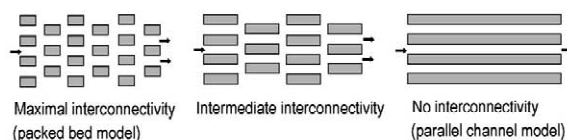

Fig. 1. Schematic representation of the different degrees of flow path interconnectivity in a chromatographic column.
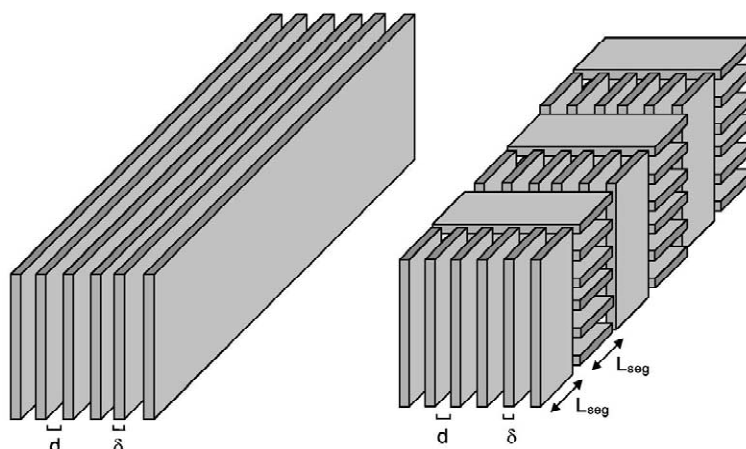
Fig. 2. Schematic view of the considered conceptual parallel plate column (a) and the segmented parallel plate column (b).

lem, and allowing for a relatively easy estimation of the additional pressure drop and band broadening induced by the presence of the segment interfaces. To calculate the velocity field and the degree of axial dispersion inside the coupling junctions, so-called computational fluid dynamics (CFD) simulations have been used. Due to the increased computational power, and the commercialization of ready-to-use software packages, CFD has become widely accepted as a design tool in the fields of hydro- and aerodynamics and chemical engineering for the solution of flow problems in complex geometries [21,22]. The basis of each CFD package is the division of the flow domain into a large number of computational cells, forming the so-called grid, followed by the use of a numerical solver to solve the Navier–Stokes equations in each of the computational cells. By solving the Navier–Stokes equations (which fully determine the velocity field) together with the appropriate mass balances, it is possible to calculate the spatial and temporal evolution of an injected plug of tracer species. Since the flows in the present problem are strictly laminar, the solution can be made 100% accurate and reliable [22]. The only requirement is that the grid is sufficiently refined, a condition which is verified by comparing the solution at two different levels of grid refinement.

In a more general sense, the results of the present study will provide insight in the optimal degree of flow path interconnectivity in LC columns (cf. Fig. 1). This insight can then for example be used to provide guidelines for the manufacturing of improved monolithic columns. In this respect, it would for example be interesting to know whether it would be more advantageous to produce column packings consisting of short (more cubic-like) and maximally interconnected voids, or whether it would be more preferable to have more elongated, longitudinally directed flow-through pores.

2. Definition of the column geometry and of the considered optimisation problem

2.1. Geometrical lay-out of the considered problem

Whereas most authors investigating multiple capillary columns considered arrays of cylindrical capillaries [20], we have preferred to focus on an imaginary column consisting of an array of flat-rectangular channels (Fig. 2a). From a practical viewpoint, these arrays should best be looked upon as a multitude of narrow slits running through a monolithic block of porous material (Fig. 3). The slits are assumed to have a width (w) which is orders of magnitude larger than their thickness (d), such that the expressions for the pressure drop and the theoretical plate height in the individual channels can be taken directly from the literature [23,24] on OT-LC in channels with a flat-rectangular cross-section. The porous structure, with wall thickness δ, serves at the same time as the stationary phase and as the
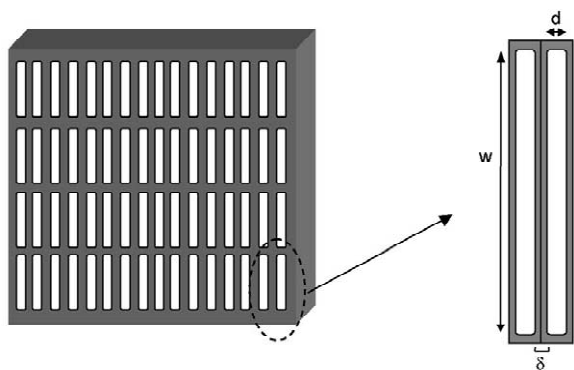
Fig. 3. Detailed view of the cross-sectional lay-out of a single block segment, consisting of a porous ''backbone'' structure (thickness δ), perforated by an array of parallel flow-through slits (thickness d).

''backbone'' providing the required mechanical strength for the segment blocks (Fig. 3). The currently considered segmented column structure can then simply be viewed upon as a stack of different segment blocks, alternately rotated over an angle of 90° (cf. Figs. 2b and 3). The square shape of the column cross-section (Fig. 3) is quite uncommon, but it is a logic consequence of the internal architecture of the packing, and also offers a number of advantages for on-column optical detection.

The advantage of the structure depicted in Figs. 2 and 3 is fourfold: (i) the resulting mathematical expressions are simple, allowing to maintain a maximal insight in the dynamics of the problem, (ii) as the capillary walls serve at the same time as the stationary phase layer, the structure is inherently more compact than the array of cylindrical capillaries, (iii) the connection and flow redistribution problem can (at least in theory) very easily be solved by piling up the different segments, alternately rotated over an angle of 90° (cf. Fig. 2b), and (iv) by varying the segment length between say one channel diameter unit and several hundreds of channel diameter units, the full range of possible degrees of flow path interconnectivity (cf. Fig. 1) can be explored and the optimal segment length (L_{seg}) can easily be determined.

As the influence of the shape of the channel cross-section on the separation efficiency is only of secondary importance, it is straightforward to assume that the results derived for the structure in Fig. 2

will, at least in a qualitative way, be extrapolatable to other possible channel cross-section geometries, including circular capillaries.

Due to the large required computational effort, we have only considered the case wherein the channel thickness d and the stationary phase plate thickness δ are both equal to 2 µm. The reasons for this choice are plural. First of all, we believe that these values are within reach of the currently available practical manufacturing possibilities (see Section 4.3). Secondly, by selecting the plate thickness slightly smaller than the particle diameter typically used in HPLC, the $d=\delta=2$ µm case also offers a (slightly) enhanced stationary phase mass transfer. Thirdly, since $\delta/d=1$ for the presently considered case, we look at a system with a column porosity of $\epsilon=0.5$ and a phase ratio $V_s/V_m=1$. These values are sufficiently close that of HPLC (where $V_s/V_m \cong 1.5$), such that it can be argued that the presently considered column structure will yield a mass loadability and a detection limit of the same order as that of a conventional HPLC column. By considering more open column structures, e.g., with a $\delta/d=V_s/V_m$ ratio of 0.2 or 0.1, better separation efficiencies and pressure drop characteristics would be obtained, but, considering that for a given k the maximal peak concentration C_{max} is linearly dependent on the phase ratio ($C_{\text{max}} \sim V_s/V_m$ [25]), the detection limits of such a column would be too far away from the current HPLC standard.

To reduce the computational effort, and to keep the mathematical expressions as simple as possible, the following assumptions have been made:

(i) Random redistribution of channel diameters after each junction, i.e., when following the path of a given fluid element, it is assumed that the diameter of the channel it enters when coming into a new segment is independent of the diameter of the channel it was occupying in the preceding segment.

(ii) Variations of the stationary phase thickness δ and the retention factor k can be neglected.

(iii) Local variations of the thickness within the same flow-through channel can be neglected.

(iv) The values for $\sigma^2_{\text{t,junc}}$ and ΔP_{junc} are identical for each individual channel and can be calculated on the basis of the mean channel thickness values d_{m} and u_{m}.

(v) The additional peak broadening coming from

the shorter sides of the flow-through channels, as for example described in Refs. [23] and [26], can be neglected.

(vi) The possible diffusive re-equilibration across the porous stationary phase plates can be neglected.

According to the work of Ding [19] and Schisla et al. [20], the assumption in (ii) does not create a significant error. This can be understood from the fact that the probability that the effects of the variation of d and δ on k outweigh each other is similar to the probability that they amplify each other. Assumption (iii) had to be made to keep the required computational effort for the CFD calculations within reasonable limits, but it can be argued that the effect of a thickness variation within the same channel will certainly not be larger than the channel-to-channel variance effect, and can in fact be considered as already being partly contained in it. Assumption (v) is based on the fact that the side-wall effect only becomes significant after a relatively large entrance length ($L > uw^2/D_{mol}$ [27]), which typically is of the order of 1 cm or more, i.e., sufficiently longer than the presently considered segment lengths. Assumption (vi) leads to an underestimation of the column performance and is hence not critical.

2.2. Calculation of the polydispersity effect

Before attacking the actual optimisation problem, we first have to quantify the additional peak broadening caused by the polydispersity effect in the reference system (i.e., the unsegmented column of Fig. 2a). To this end, we followed a procedure similar to the one used by Schisla et al. [20]. The main difference is that we consider an array of flat-rectangular channels, whereas they considered the case of an array of circular capillaries. Their calculation is based on writing the concentration elution profile for each individual channel as:

$$C_1(t) = \frac{M}{\Omega L} \cdot \frac{t_R}{\sqrt{2\pi} \cdot \sigma_t} \cdot e^{-\frac{(t-t_R)^2}{2\sigma_t^2}} \tag{1}$$

wherein t_R is the mean residence time of a given component in a given channel:

$$t_R = \frac{L}{u_1} \cdot (1+k) \tag{2}$$

and wherein σ_t^2 is the peak variance in the same given channel. For a flat-rectangular channel with large w/d ratio, and by neglecting the side-wall effect, σ_t^2 is known [24] to be given by:

$$\sigma_t^2 = 2D_m \cdot (1+k)^2 \cdot \frac{L}{u_1^3} + \frac{2}{210} \cdot (1 + 9k + 25.5k^2)$$

$$\cdot \frac{d^2}{D_m} \cdot \frac{L}{u_1} + \frac{2}{3} \cdot k \cdot \frac{d_f^2}{D_s} \cdot \frac{L}{u_1} \tag{3}$$

The velocity in each individual channel is determined by Poiseuille's law, which for a channel with a flat-rectangular cross-section is given by [28]:

$$u_1 = \frac{\Delta P}{12\mu L} \cdot d^2 \tag{4}$$

Schisla et al. [20] further assumed that the thickness d of the individual channels varies according to a Gaussian distribution f with mean d_m and variance σ_d^2:

$$f(d) = \frac{1}{\sqrt{2\pi} \cdot \sigma_d} \cdot e^{-\frac{(d-d_m)^2}{2\sigma_d^2}} \tag{5}$$

Introducing the variables x and σ_x such that:

$$d = d_m(1+x) \quad \text{and} \quad \sigma_x = \sigma_d/d_m \tag{6}$$

Eq. (5) can be rewritten in a dimensionless form as:

$$f(x) = \frac{1}{\sqrt{2\pi} \cdot \sigma_x} \cdot e^{-\frac{x^2}{2\sigma_x^2}} \tag{7}$$

while the expression for the velocity in each individual channel can be written as:

$$u(x) = \frac{\Delta P d_m^2}{12\mu L} \cdot (1+x)^2 = u_m \cdot (1+x)^2 \tag{8}$$

Averaging the velocity over the different channels then corresponds to calculating:

$$\langle u \rangle = \frac{\int_{-\infty}^{+\infty} w \cdot d(x) \cdot u(x) \cdot f(x) \cdot dx}{\int_{-\infty}^{+\infty} w \cdot d(x) \cdot f(x) \cdot dx} \tag{9}$$

Using Eqs. (A.7a)–(A.7c) and (A.8a)–(A.8c) of Appendix A, solving Eq. (9) yields:

$$\langle u \rangle = \frac{\Delta P d_m^2}{12 \mu L} \cdot \left(1 + 3\sigma_x^2\right) = u_m \cdot \left(1 + 3\sigma_x^2\right) \qquad (10)$$

The fact that the mean velocity is larger than that expected on the basis of the mean channel thickness d_m follows directly from the fact that, since the flow-rate $\sim wd^3$, channels with a thickness which is larger than the mean thickness have a relatively larger contribution to the total flow-rate than channels with a smaller thickness.

According to Ref. [20], averaging the residence time over all the individual capillaries corresponds to:

$$\langle t_R \rangle = \frac{M_1}{M_0}$$

$$= \frac{\int_{-\infty}^{+\infty} w \cdot d(x) \cdot u(x) \cdot \left[\int_0^{+\infty} t C_1(x,t) \cdot dt\right] \cdot f(x) \cdot dx}{\int_{-\infty}^{+\infty} w \cdot d(x) \cdot u(x) \cdot \left[\int_0^{+\infty} C_1(x,t) \cdot dt\right] \cdot f(x) \cdot dx}$$

$$(11)$$

while the overall variance of the peak profile recorded when simultaneously monitoring the output of all the individual channels should be calculated according to:

$$\langle \sigma_t^2 \rangle = \frac{M_2}{M_0} - \left(\frac{M_1}{M_0}\right)^2$$

$$= \frac{\int_{-\infty}^{+\infty} w \cdot d(x) \cdot u(x) \cdot \left[\int_0^{+\infty} t^2 C_1(x,t) \cdot dt\right] \cdot f(x) \cdot dx}{\int_{-\infty}^{+\infty} w \cdot d(x) \cdot u(x) \cdot \left[\int_0^{+\infty} C_1(x,t) \cdot dt\right] \cdot f(x) \cdot dx}$$

$$- \langle t_R \rangle^2$$

$$(12)$$

As is demonstrated in Appendix A, solving Eqs. (11) and (12), respectively, yields:

$$\langle t_R \rangle = \frac{L}{u_m} \cdot (1 + k) \cdot \left(1 + \sigma_x^2 + 3\sigma_x^4\right) \qquad (13)$$

$$\langle \sigma_t^2 \rangle = A' \cdot \frac{L}{u_m^3} + B' \cdot \frac{L}{u_m} + C' \cdot \frac{L}{u_m} + D' \cdot \frac{L^2}{u_m^2} \qquad (14)$$

The validity of the numerical expressions for $\langle t_R \rangle$ and $\langle \sigma_t^2 \rangle$ given by Eqs. (13) and (14) and Eqs.

(A.9)–(A.12) has been verified by numerically solving the integrals given in Eqs. (11) and (12). Another, more qualitative validation of the presented result is that, when taking the limit for $\sigma_x \rightarrow 0$, the D-term representing the polydispersity effect vanishes (cf. Eq. (A.12)). The fact that the D' term in Eq. (14) is proportional to L^2 implies that it imposes an upper limit to the achievable plate number, a limit which cannot be surpassed by increasing the length of the column or the inlet pressure. It is precisely this outcome which makes the polydispersity effect so devastating for the column performance.

In a more qualitative way, the polydispersity problem can be understood as a problem of synchronisation. If one is after 10^4 or 10^6 plates, the peak standard deviations are only 1 to 0.1% of the mean residence time (cf. $\sigma_t = N^{1/2} t_R$). This implies that the velocities in the different channels should also be synchronised to within 0.1 to 1%. Since the velocity depends on the square of the channel diameter, this implies that the differences in channel thickness should be smaller than 0.5 to 0.05% to avoid the channel polydispersity effect. For a 2 μm channel for example, the 0.5% condition corresponds to an extremely small value of only 10 nm [29].

Fig. 4 shows the solute concentration profile eluting from a parallel flat plate column for several
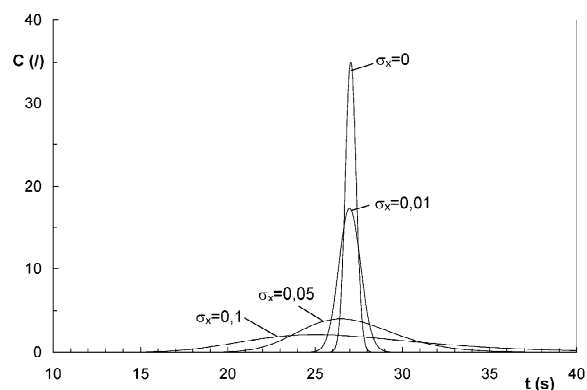
Fig. 4. Eluting profile from a parallel-bundle-of-flat-plates column for several values of the channel-to-channel thickness variance σ_x. Curves are calculated using Eqs. (1)–(3) and (7)–(8). Simulation parameters: $d = 2$ μm, $\delta = 2$ μm, $L = 0.3$, $d_f = 1$ μm, $D_m = 1 \cdot 10^{-9}$ m^2/s, $D_s = 5 \cdot 10^{-10}$ m^2/s, $\mu = 1 \cdot 10^{-3}$ kg/(m s), $k = 3$, $\Delta P = 400$ bar, $u \equiv 4.44$ cm/s.

values of σ_x and for a typical set of LC conditions. The devastating effect of the polydispersity can clearly be noted. The curves were obtained by numerically calculating the flow-rate averaged concentration over all the different channel thickness values of an array with a Gaussian thickness distribution, using Eqs. (1)–(3) to calculate the concentration profile in each individual channel, and using Eq. (7) as a weight factor for the different channel thickness values of the array. Calculating the σ_t^2 values of the presented concentration curves, the obtained values agree to within 0.1% to the value predicted by Eq. (14), hence confirming the validity of the latter. Translating the σ_t^2 values into a theoretical plate number, the resolution ruining effect of the channel thickness polydispersity can be clearly illustrated. Whereas the ideal column with a perfectly uniform channel thickness ($\sigma_x = 0$) should yield a separation resolution of $N = 7660$ plates (conditions: see figure caption), a 1% polydispersity already decreases the separation resolution to a value of $N = 1880$ plates, while a 5 and a 10% polydispersity lead to a dramatic plate loss: $N = 97$ plates for $\sigma_x = 0.05$ and $N = 23$ plates for $\sigma_x = 0.1$, respectively. According to the calculations of Schisla et al. [20], even larger plate losses would have been obtained when we would have selected a mobile phase velocity near the u_{opt} value instead of the presently considered maximal velocity of about $u = 4.4$ cm/s, corresponding to a maximal pressure drop of 400 bar.

2.3. Theoretical expression for H and N_{max} for the segmented column

Considering now the segmented column depicted in Fig. 2b, and denoting the total pressure drop, residence time and peak variance in each segment as ΔP_{seg}, $t_{R,seg}$ and $\sigma_{t,seg}^2$, respectively, and denoting the additional pressure drop and peak broadening caused by the coupling junction as ΔP_{junc} and $\sigma_{t,junc}^2$, it is obvious that the overall pressure drop, residence time and peak variance for the entire segmented column (consisting of n_s segments) are, respectively, given by:

$$\Delta P = n_s \Delta P_s + (n_s - 1)\Delta P_{junc} \tag{15}$$

$$t_R = n_s t_{R,seg} \tag{16}$$

$$\sigma_t^2 = n_s \sigma_{t,seg}^2 + (n_s - 1)\sigma_{t,junc}^2 \tag{17}$$

The quantities $t_{R,seg}$ and $\sigma_{t,seg}^2$ can simply be calculated by putting $L = L_{seg}$ in Eqs. (13) and (14). At this point, it is instructive to note that the advantage of the segmented column is reflected by the fact that the D term in Eq. (14) now only is proportional to L_{seg} instead of to the whole column length L. Similarly, the pressure drop ΔP_{seg} across each segment of length L_{seg} can, from the expression for the average flow velocity (cf. Eq. (10)), be written as:

$$\Delta P_{seg} = \frac{12\mu \cdot \langle u \rangle \cdot L_{seg}}{(1 + 3\sigma_x^2) \cdot d_m^2} = \frac{12\mu u_m L_{seg}}{d_m^2} \tag{18}$$

From Eqs. (13)–(17), the number of theoretical plates N which can be achieved in a segmented column with length $L = n_s L_{seg}$ can now be calculated as:

$$\frac{1}{N} = \frac{\langle \sigma_t^2 \rangle}{\langle t_R \rangle^2}$$

$$= \left[\frac{n_s \sigma_{t,seg}^2}{n_s^2 L_{seg}^2} + \frac{(n_s - 1)\sigma_{t,junc}^2}{n_s^2 L_{seg}^2} \right]$$

$$\cdot \frac{u_m^2}{(1+k)^2 \cdot (1 + \sigma_x^2 + \sigma_x^4)^2} \cdot \frac{1}{N} = \frac{\langle \sigma_t^2 \rangle}{\langle t_R \rangle^2}$$

$$= \left[n_s \cdot \left(A' \cdot \frac{L_{seg}}{u_m^3} + B' \cdot \frac{L_{seg}}{u_m} + C' \cdot \frac{L_{seg}}{u_m} + D' \right. \right.$$

$$\left. \cdot \frac{L_{seg}^2}{u_m^2} \right) + (n_s - 1)\sigma_{t,junc}^2 \right]$$

$$\cdot \frac{u_m^2}{L^2(1+k)^2 \cdot (1 + \sigma_x^2 + \sigma_x^4)^2} \tag{19}$$

Integrating the factor $(1+k)^2 \cdot (1 + \sigma_x^2 + \sigma_x^4)^2$ into the newly introduced symbols A'', B'', C'' and D'', and replacing L_{seg} by L/n_s, Eq. (19) becomes:

$$\frac{1}{N} = \frac{\langle \sigma_{\mathrm{t}}^2 \rangle}{\langle t_{\mathrm{R}} \rangle^2}$$

$$= \left[\left(\frac{A''}{u_{\mathrm{m}}} + (B'' + C'')u_{\mathrm{m}} + D'' \cdot \frac{L}{n_{\mathrm{s}}} \right) \cdot L \right.$$

$$\left. + (n_{\mathrm{s}} - 1)\sigma_{\mathrm{t,junc}}^2 u_{\mathrm{m}}^2 \right] \cdot \frac{1}{L^2} \qquad (20)$$

Eq. (20) shows that, in a segmented column with given length L, the D'' term representing the polydispersity effect can, as expected, indeed be eliminated by creating an infinite number of channel redistributions (i.e., by letting $n_{\mathrm{s}} \to \infty$). This effect is of course countered by the fact that the $\sigma_{\mathrm{t,junc}}^2$ term increases in a proportional way with n_{s}. Eq. (20) hence clearly reflects the existence of an optimal degree of column segmentation or channel connectivity.

From Eq. (20), the theoretical plate height value H is immediately obtained as:

$$H = \frac{L}{N} = \frac{A''}{u_{\mathrm{m}}} + (B'' + C'')u_{\mathrm{m}} + D'' \cdot \frac{L}{n_{\mathrm{s}}} + \frac{(n_{\mathrm{s}} - 1)}{L}$$

$$\cdot \sigma_{\mathrm{t,junc}}^2 u_{\mathrm{m}}^2 \qquad (21)$$

Assuming that n_{s} is large enough to have $n_{\mathrm{s}} - 1 \cong n_{\mathrm{s}}$, Eq. (21) reduces to:

$$H = \frac{L}{N}$$

$$= \frac{A''}{u_{\mathrm{m}}} + (B'' + C'')u_{\mathrm{m}} + D''L_{\mathrm{seg}} + \frac{\sigma_{\mathrm{t,junc}}^2 u_{\mathrm{m}}^2}{L_{\mathrm{seg}}} \qquad (22)$$

As increasing the number of coupling junctions also increases the total pressure drop and hence limits the allowable column length, the calculation of the maximally achievable plate number N_{max} requires that Eq. (20) should be considered together with the relation between the achievable column length L and the available pressure drop ΔP. Rewriting Eq. (15) as:

$$\Delta P = u_{\mathrm{m}} \cdot [n_{\mathrm{s}} R_{\mathrm{seg}} L_{\mathrm{seg}} + (n_{\mathrm{s}} - 1) \cdot R_{\mathrm{junc}}] \qquad (23a)$$

this relation can be written as:

$$L = n_{\mathrm{s}} L_{\mathrm{seg}} = \frac{1}{R_{\mathrm{seg}}} \cdot \left[\frac{\Delta P}{u_{\mathrm{m}}} - (n_{\mathrm{s}} - 1) \cdot R_{\mathrm{junc}} \right] \qquad (23b)$$

Eqs. (20) and (23) now form a closed set of equations allowing to calculate the maximal number of theoretical plates N_{max} which can be achieved with a segmented parallel plate column. From Eq. (23), it can also easily be shown that, since of course $L > 0$, the upper limit ($n_{\mathrm{s,max}}$) on the number of segments into which the column can be divided is given by:

$$n_{\mathrm{s,max}} = 1 + \frac{\Delta P}{R_{\mathrm{junc}} u_{\mathrm{m}}} = 1 + \frac{\Delta P}{\Delta P_{\mathrm{junc}}} \qquad (24)$$

3. Computational fluid dynamics calculations

To actually calculate the achievable plate numbers and to determine the optimal number of channel segments from Eqs. (20) and (23), the additional pressure-drop ΔP_{junc} and peak variance $\sigma_{\mathrm{t,junc}}^2$ introduced by the coupling junctions have to be accurately known. To determine these values, flow and tracer dispersion simulations were performed with a Fluent CFD software (version 6.0.20) package, run in parallel on a Compaq XP 1000 workstation with an Alpha 667 Mhz processor and on several personal computers with 1.5 Ghz Intel Pentium IV or dual-Athlon MP 1800 processors.

Calculating the entire segmented column depicted in Fig. 2b is a task which is much too formidable for the current state-of-the art computer processors. However, as the column consists of a continuous repetition of the same basic structure, it is sufficient to calculate only a small representative element of the column (see Fig. 5). To further reduce the calculation domain, the walls denoted by ''slip wall'' in Fig. 5 were treated as ''slip walls'', i.e., a flow symmetry condition is imposed. In this way, the intersecting channel elements depicted in Fig. 5 behaved as if they were infinitely wide in the y direction (section I), and the x direction (section II), respectively.

For each considered problem, we first solved the steady state flow problem, yielding the solution for the velocity profile and allowing to assess the total pressure drop. The velocity field solution was then fed into the mass balance solver to calculate the
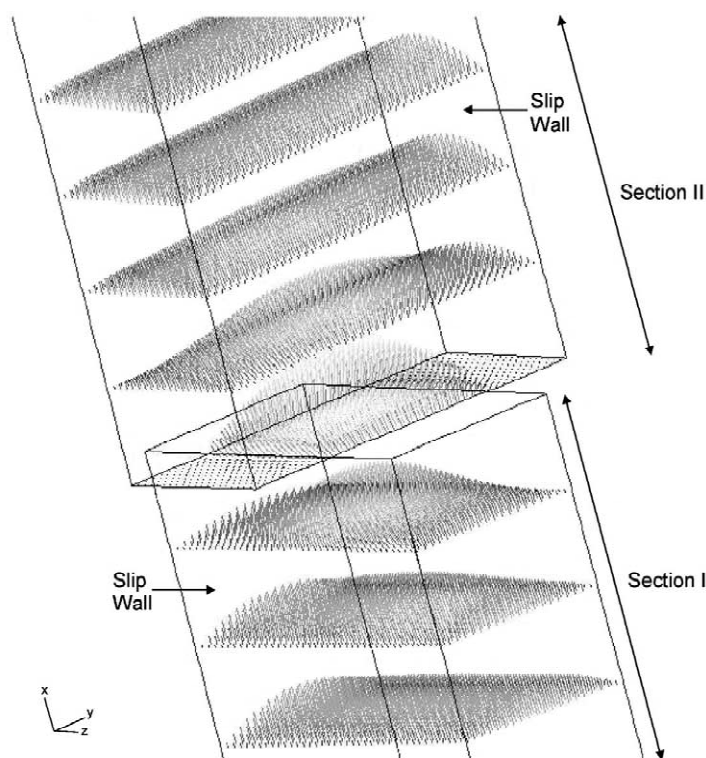
Fig. 5. Three-dimensional view of the considered segmented column element [$u_m = 9$ mm/s, $d = 2$ μm, $\delta = 2$ μm, $L_I = L_{II} = 15$ μm, $\mu = 1 \cdot 10^{-3}$ kg/(m s), $D_m = 1 \cdot 10^{-9}$ m^2/s], showing the calculated velocity field (black arrows).

evolution of an injected tracer band through the coupling section. Whereas the solution of the velocity field only takes a few hours, depending on the grid refinement and the required accuracy, the solution of the unsteady mass balances takes much longer. Even with the above mentioned drastic simplifications, it still took the Compaq work station typically about 1 week to calculate the entire tracer plug trajectory for the case with $d = 2$ μm and $u = 3$ mm/s. For smaller values of d, the simulations became extremely long. It was found that the required computation time to solve the mass balance increased in a nearly quadratic way with $1/d$.

The number of computational cells was about 60 000 in each of the considered geometries. A grid check was performed with a grid containing 480 000 cells for the case of $d = 2$ μm and $u = 3$ mm/s, and the difference between the obtained $\sigma^2_{t,junc}$ values was only of the order of 1%.

4. Results and discussion

4.1. Pressure drop and axial dispersion data from the CFD study

Fig. 5 shows the calculated velocity magnitude field for one of the considered flow cases. We clearly observe two stagnant zones, just prior and just after the coupling section. This is fully expected, because the flow situation at these positions is respectively very similar to the situation just prior to a sudden reduction and just after a sudden expansion of the cross-section of an open-tubular channel. It should be recalled that in section I (extending infinitely in the z direction), the flow displays a parabolic gradient in the y direction but is gradient-less in the z direction, whereas in section II (extending infinitely in the y direction), the flow displays a parabolic gradient in the z direction and is gradient-less in the

y direction. In the smaller "window" of the coupling junction, the flow profile displays a rotational symmetry and has a gradient in both the *y* and the *z* directions. The passage through the coupling section should hence be regarded as a transition process between a flow with one-dimensional (1D) parabolic flow profile in the *y* direction towards a flow with a 1D parabolic flow profile in the *z* direction.

Fig. 6a shows the evolution of the shape of an injected (block-shaped) solute band when passing through the coupling section. Fig. 6b shows the concentration curves which are "recorded" at the different monitoring planes indicated in Fig. 6a. For the sake of comparison, we have also included the concentration profiles which would be obtained if the

two channel segments I and II in Fig. 5 would be rotated such that they form a single, straight running channel without coupling interface. As can be noted, the influence of the coupling is relatively small. By calculating the variance σ_t^2 of the concentration curves given in Fig. 6b, the degree of band broadening can readily be quantified. Fig. 7 shows how these σ_t^2 values vary with the distance along the *x* coordinate. The evolution of the pressure-profile is given as well. The influence of the coupling interface can clearly be noted. The dashed lines represent the relationship which would be obtained for a peak flowing through a fully straight channel, without coupling interface. The fact that the σ_t^2 curve goes through a maximum at the position of the coupling
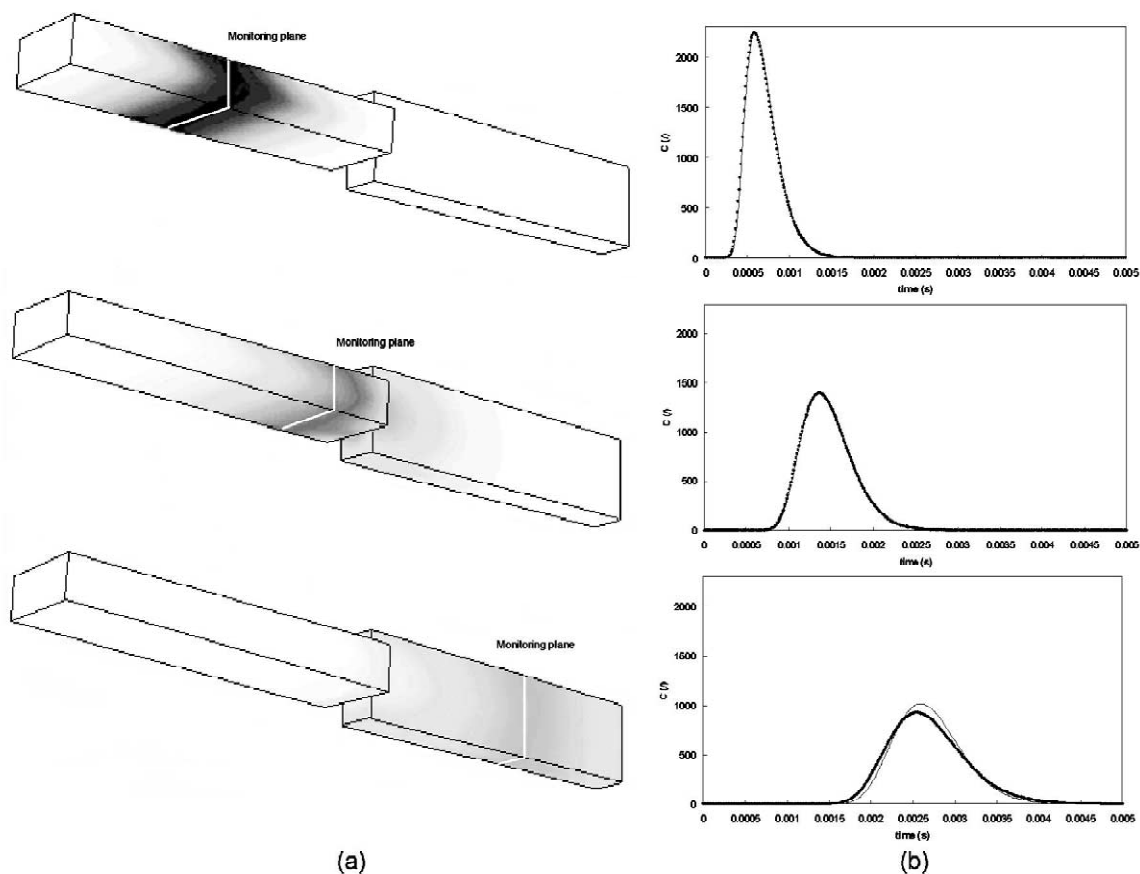

Fig. 6. (a) Evolution of the shape of an injected solute band flowing through the coupling section (black zones = largest concentration). (b) Dotted thick line: spatially averaged solute concentration curves "recorded" at the different peak monitoring planes indicated in (a). The thin black line represent the curves which would be obtained for a peak flowing through a fully straight channel, i.e., without coupling interface. Conditions as in Fig. 5.
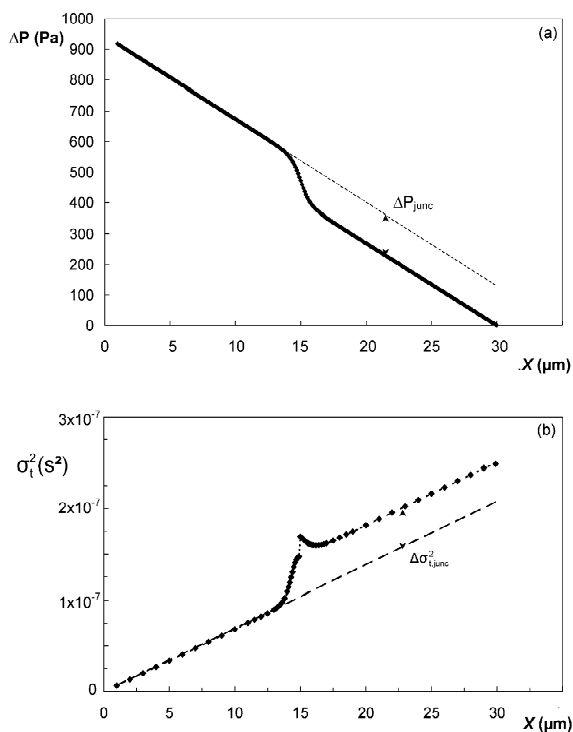
Fig. 7. Calculated pressure-drop (a) and σ_t^2 profiles (b) for the case represented in Fig. 6. The dashed lines represent the theoretically predicted σ_t^2 and ΔP values for an unobstructed straight channel.

plane, and decreases with increasing x in the first few micrometers behind the coupling can be explained from the fact that the transition between the two-dimensional (2D) parabolic flow profile (gradients in both y and z directions) in the coupling window to a flow which is gradient-less in the y direction (far enough downstream in section II) is accompanied by a spreading of the tracer plug in the y direction. This spreading process reduces the axial width of the tracer plug, hence explaining the local decrease of the σ_t^2 values.

As indicated in Fig. 7a, the additional pressure drop ΔP_{junc} introduced by the coupling section can easily be calculated. Repeating the simulation presented in Figs. 5–7 for a number of different flow velocities and channel thickness values, the resulting ΔP_{junc} correlations displayed a perfect straight line correlation with both the mobile phase velocity and the reciprocal of the channel thickness (Fig. 8). The data could be correlated as:
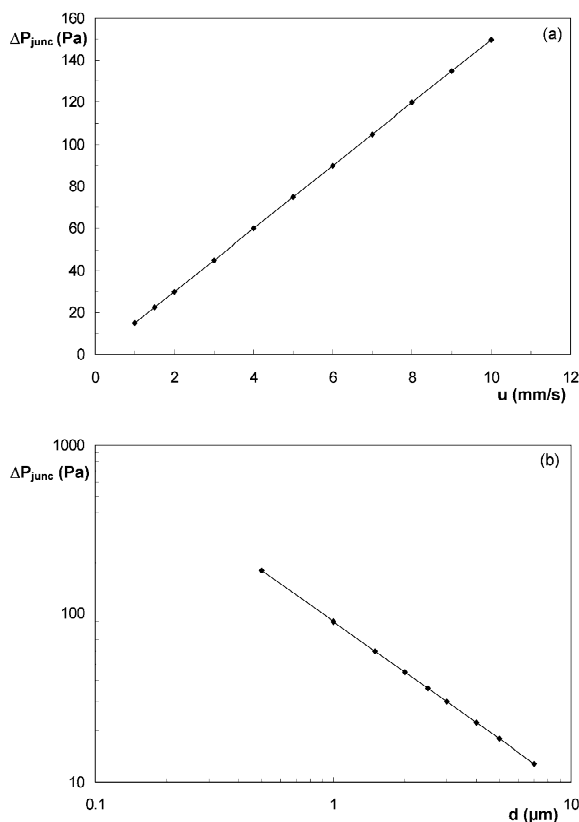

Fig. 8. Variation of ΔP_{junc} as a function of the mean fluid velocity u_m for the case of $d = \delta = 2$ μm (a) and ΔP_{junc} as a function of the channel thickness d for the case of $u = 3$ mm/s and $\delta = 2$ μm (b).

$$\Delta P_{junc} = \alpha \cdot \frac{\mu u_1}{d} = R_{junc} u_1 \qquad (25)$$

with $\alpha = 29.84$ (± 0.01) and $R_{junc} = 1.496 \cdot 10^4$ kg/(m^2 s) (± 10 kg/(m^2 s)

It should be noted that α is of course not a universal value, but strongly depends on the cross-sectional area of the junction surface S_{junc} available for the fluid flow. In general, the relation between the surface of the coupling window and the dimensions of the channel and wall plate thickness is given by:

$$S_{junc} = d \cdot \left(\frac{d}{d+\delta} \cdot w \right) = \frac{dw}{1 + \dfrac{\delta}{d}} \qquad (26)$$

For the presently considered case of $\delta = d$, Eq. (26) reduces to $S_{junc} = 1/2 \cdot dw$.

The result in Eq. (25) is in agreement with known

correlations for the pressure drop for the flow through pipes with sudden geometry changes, for which it is usually found that [30]:

$$\Delta P = 2\rho f_F u^2 K_1 \qquad (27)$$

wherein K_1 is a given constant, dependent on the geometry of the problem, and wherein f_F is the friction factor, normally being inversely proportional to the Reynolds number in the laminar flow regime [30]:

$$f_F = K_2/\mathrm{Re} = K_2 m/(u d \rho) \qquad (28)$$

Combining Eqs. (27) and (28) indeed yields an expression of the form of Eq. (25). Putting $\alpha = 2K_1 K_2$, and considering that $K_2 = 12$ for a laminar flow between two parallel plates, we can derive from the $\alpha = 29.8$ value given in Eq. (25) that the value for K_1 for the presently considered geometry is about $K_1 = 1.25$, i.e., significantly smaller than the values given in the literature for the pressure-drop in a pipe with a sudden decrease or increase of the cross-section, and typically of the order of 10 to 50 [30]. The low K_1 value points at the excellent pressure-drop characteristics of the presently proposed coupling system, and can easily be understood from the fact that the present junction system is designed such that the region over which the cross-sectional area is temporarily increased or decreased (going from a value of $S = wd$ to the value given in Eq. (26)) is infinitely short, whereas in the cases leading to the above mentioned values of $K_1 = 10$ to 50, the reduced or increased channel cross-section persists over the entire remainder of the channel length.

Fig. 9 shows the evolution of the peak variance $\sigma_{t,\mathrm{junc}}^2$ originating from the coupling junction as a function of the imposed mobile phase velocity. It was found that the relation between $\sigma_{t,\mathrm{junc}}^2$ and u does not follow a pure power-law correlation with integer exponential. The reason for this is that the additional peak broadening induced by the passage through the coupling junction is the result of two different, and even counteracting phenomena (diffusive exchange with stagnant zones and reorientation of a parabolic velocity gradient), as mentioned in the discussion of Figs. 5 and 6. The best fitting expression for the data points in Fig. 9 was found to be given by:
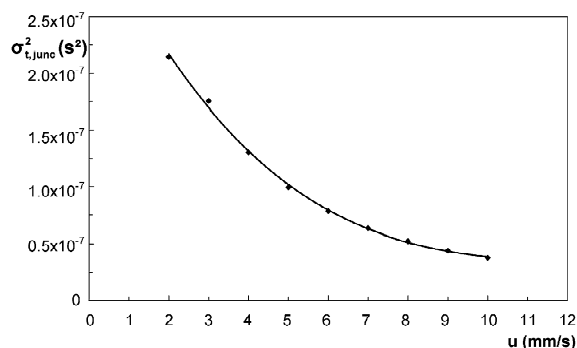

Fig. 9. Variation of $\sigma_{t,\mathrm{junc}}^2$ as a function of the mean fluid velocity u for the case of $d = \delta = 2$ μm.

$$\sigma_{t,\mathrm{junc}}^2 = 3.2 \cdot 10^{-7} \cdot \mathrm{e}^{-220u} \quad (\text{units} = \mathrm{s}^2) \qquad (29)$$

It should of course again be noted that the constants in Eq. (29) values are only valid for the presently considered geometry.

4.2. Chromatographic performance

All the data in the present section have been obtained for a set of typical LC condition values: $k = 3$, $D_m = 10^{-9}$ m^2/s, $D_s = 5 \cdot 10^{-10}$ m^2/s, $\mu = 1 \cdot 10^{-3}$ kg/(m s) and $\Delta P = 400$ bar. For the segmented parallel plate column, all values refer to the case of $d = 2$ μm and $\delta = 2d_f = 2$ μm.

Fig. 10(a) shows how the maximally achievable theoretical plate number varies with the segment length L_{seg}. Fig. 10(b) shows the corresponding reduced plate heights. For the sake of comparison, we have also included the packed bed data for the case of a column with $d_p = 3$ μm, calculated using:

$$H = 2\lambda d_p + 2\gamma \cdot \frac{D}{u} + \frac{0.37 + 4.96k + 4.04k^2}{(1+k)^2} \cdot u \cdot \frac{d_p^2}{D_m} \qquad (30)$$

[31] and:

$$u = \frac{\Delta P d_p^2}{\psi L \mu} \quad (\psi = 750) \qquad (31)$$

It should be noted that the N_{max} values given in Fig. 10(a) have been obtained by selecting the corresponding optimal mobile phase velocity $u_m =$
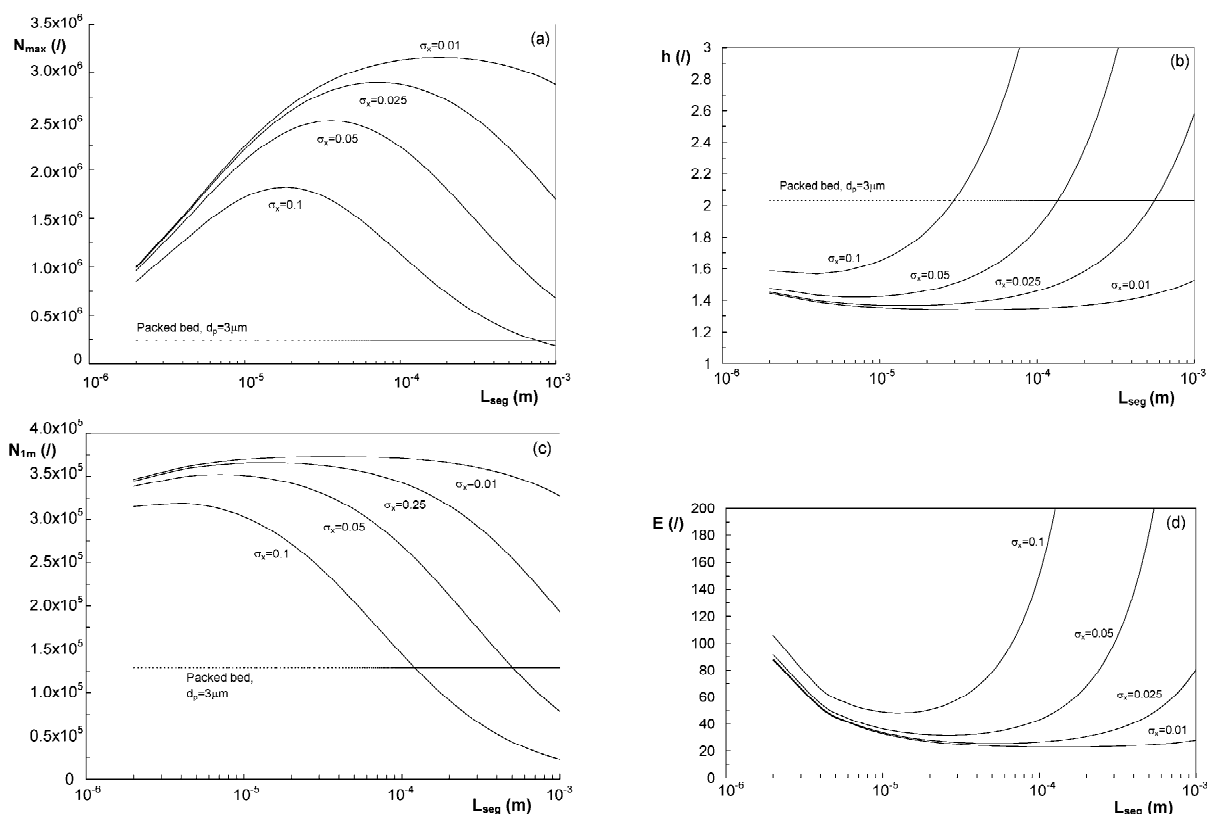
Fig. 10. (a) Variation of N_{max} with L_{seg} for the segmented parallel plate column for different values of σ_x and comparison with HPLC column with $d_p = 3$ μm and $\psi = 750$; (b) variation of corresponding reduced plate height h; (c) variation of number of plates ($N_{1\ m}$) achievable in a 1 m column; and (d) corresponding separation impedance values. Conditions: $d = 2$ μm, $\delta = 2$ μm, $D_m = 1 \cdot 10^{-9}$ m^2/s, $D_s = 5 \cdot 10^{-10}$ m^2/s, $\mu = 1 \cdot 10^{-3}$ kg/(m s), $\Delta P = 400$ bar, $k = 3$, $\psi = 750$.

$u_{m,opt}$ (obtained by numerically varying u_m to find the maximal N for the given L_{seg} and ΔP) for each considered value of L_{seg}. In this way, we were certain to obtain the solution with the largest possible N, and it also allowed to eliminate one variable from the solution space. It should also be noted that the N_{max} data presented in Fig. 10(a) correspond to column lengths ranging from about $L = 2.7$ m for the smallest considered L_{seg} values to about $L = 9$ m for the largest L_{seg} values. To neutralize the column length factor, we have divided the N_{max} values given in Fig. 10(a) by the corresponding column length. These values, yielding the number of plates $N_{1\ m}$ achievable in a column with a length of 1 m (which seems to be the practical limit for a segmented monolithic plate column), are given in Fig. 10(c). Fig. 10(d) shows the corresponding values of the

separation impedance factor introduced by Knox [15,32]:

$$E = \frac{\Delta P}{N\mu} \cdot \frac{t_0}{N} = \frac{H^2}{B_0} = h^2 \psi \tag{32}$$

Fig. 10(a), clearly confirms the expected (cf. Eq. (20)) existence of an optimal L_{seg} value. As can be expected, the optimal segment length increases with decreasing channel thickness variance σ_x. When comparing Fig. 10(a)–(d), the value of the optimal segment length clearly also depends upon the selected optimisation criterion. When a minimal H or a maximal N is desired, the optimal segment length goes from a value of $L_{seg,opt} = 15$ μm for $\sigma_x = 0.1$ to a value of $L_{seg,opt} = 150$ μm for $\sigma_x = 0.01$ (Fig. 10(a)). When the number of plates in a 1 m column is to be

maximised, the optimal segment length values are clearly smaller, varying from a value of $L_{seg,opt} = 4$ μm for $\sigma_x = 0.1$ to a value of $L_{seg,opt} = 25$ μm for $\sigma_x = 0.01$ (Fig. 10(c)). Also in agreement with what could be intuitively expected is that, the smaller σ_x, the larger the range of L_{seg} values over which larger N_{max} and $N_{1\,m}$ values are obtained, i.e., the larger the degree of freedom over which the segment length can be selected. For a large channel-to-channel thickness variation, the selection of L_{seg} is clearly more critical.

The most eye-catching result from Fig. 10(a) is the enormous gain in maximal plate number with respect to the packed bed of spherical particles, hence clearly confirming the assumption of Schisla et al. [20] that the polydispersity effect in a parallel open channel column can be strongly alleviated by regularly providing a flow redistribution section. The presently proposed segment coupling method clearly allows to organize this redistribution in such a way that the advantage coming from the suppression of the polydispersity effect is much larger than the losses caused by the additional pressure-drop and band broadening.

The reduced plate height values in Fig. 10(b) show that the segmented parallel plate column allows to achieve h values significantly below $h = 2$, which is generally assumed to be the "signature" of an ideally packed HPLC column, although there is no real theoretical basis to claim this [33]. The $N_{1\,m}$ data in Fig. 10(c) again show the advantage of the improved internal column architecture of the segmented parallel plate column. The difference with the packed bed is now smaller than for the N_{max} data, as the latter are more strongly affected by the flow resistance of the column than the $N_{1\,m}$ data. The values of $N_{1\,m}$ around 200 000 to 300 000 are also significantly larger than the value of about 100 000 plates which can be achieved in a 130 cm silica monolith column [1]. This points at the fact that even the performance of modern monolithic LC columns is still far away from the absolute resolution limit of a fully optimised HPLC column. This finding should stimulate further research on the development of better structured column packings.

When considering the E values presented in Fig. 10(d), the large potential kinetic advantage of the segmented parallel plate column concept is revealed

in all its virtue. The obtained minimal E values of the order of $E = 20$ to 40 are indeed dramatically lower than the value of $E = 3000$ typically cited for a good packed bed column [1]. They are even more than an order of magnitude smaller than the best values reported thus far for monolithic LC columns ($E = 400$ to 800 [1]).

The very small E values shown in Fig. 10(d) point at the large gain in analysis time which can be expected for large-N separations. This is confirmed in Fig. 11. As can be expected, the gain in analysis time offered by the segmented parallel plate column increases with increasing required plate number. It can roughly be said that the difference between the HPLC column and the segmented plate column is about a factor of 10, which is really dramatic. It should be noted that the segmented parallel plate column data do not even refer to a fully optimised column, but refer to the case of a column composed out of segments with length $L_{seg} = 100$ μm. This value has been more or less arbitrarily selected (see Section 4.3), as representing the best possible compromise between the practical manageability of the segments on the one hand and the separation resolution and speed of the column on the other hand. It should furthermore be noted that the segmented
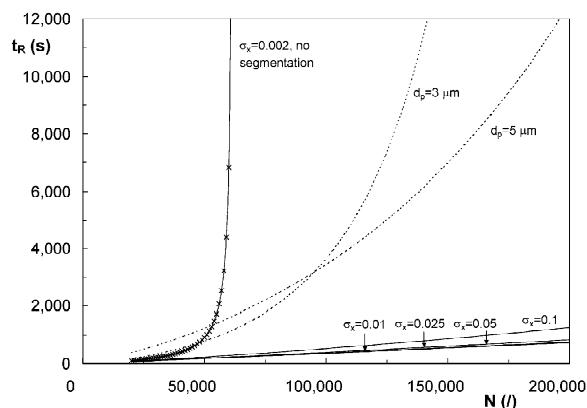

Fig. 11. Comparison of the required analysis time as a function of the theoretical plate number between a segmented parallel plate column (full lines) and a conventional packed bed column (dashed lines). The required analysis time of an unsegmented parallel plate column (with an σ_x of only $\sigma_x = 0.002$) is given as well (full line with crosses). Conditions as in Fig. 10.

column concept can even yield much shorter separation times, by for example considering a column with $d = \delta = 1$ μm instead of the $d = \delta = 2$ μm case for which the data in Fig. 11 have been obtained. To again illustrate the severity of the polydispersity effect, we have also included the analysis time data of an un-segmented column. Even by lowering the channel-to-channel thickness variance to an impractically small value of $\sigma_x = 0.002$, the required analysis time very rapidly reaches a vertical asymptote.

As the $L_{seg} = 100$ μm case for which the t_R data in Fig. 11 have been calculated is more or less selected arbitrarily, Fig. 12a–b shows how the t_R value varies with L_{seg} for a separation requiring, respectively, $N = 100\,000$ and $N = 150\,000$ plates. Similar to the

cases in Fig. 10, we again note the existence of an optimal segment length, and we again see that $L_{seg,opt}$ increases with decreasing channel-to-channel thickness variation σ_x. When comparing Fig. 12a with Fig. 12b, we also note that the $L_{seg,opt}$ value is nearly independent of the required plate number. From a practical point of view, it is also very interesting to note that there is a relatively broad region, say between $L_{seg} = 10$ μm and $L_{seg} = 200$ μm, wherein the exact value of L_{seg} is not really critical, at least not when $\sigma_x \leq 0.05$. This offers a large degree of freedom for the practical realization of the concept (see also Section 4.3). It is also interesting to note that for the considered cases of $N = 100\,000$ and $N = 150\,000$, the channel-to-channel variation does not need to be better than $\sigma_x = 0.05$. Smaller values yield no significant gain in analysis time.

Using the obtained results to evaluate the structural properties of the new polymeric and silica monolithic LC columns now being developed [10–14], the relatively sharp increase of the N_{max} and t_R curves in the range of small L_{seg} (i.e., for $L_{seg} \rightarrow d$) points at the fact that, provided the variation in flow-through pore diameter can be kept below 10%, monolithic LC columns would greatly benefit from more elongated flow-through pores, preferably extending over more than 10 times the pore diameter. When the variation on the flow-through pore diameter is however larger than say 10%, it seems better to stick to the more cubic or globular pore shape obtained with the present sol–gel and polymer–gel methods.
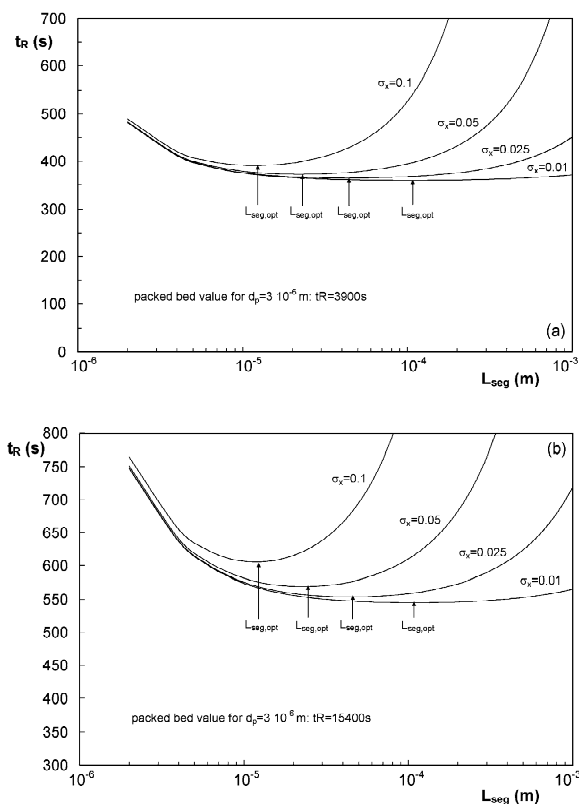

Fig. 12. Evolution of the required analysis time as a function of the channel segment length L_{seg} for different values of σ_x for a separation requiring $N = 100\,000$ plates (a) and for a separation requiring $N = 150\,000$ plates (b). Simulation conditions as in Fig. 10.

4.3. Some practical manufacturing considerations

Although the presently considered segmented parallel plate column structure should essentially be regarded as a means to gain insight in the optimal LC column design, it is nevertheless worthwhile to consider the practical feasibility of the concept. The fact that the typical optimal segment length can be more or less freely selected between say 10 to 100 μm, and the fact that the channel to channel thickness variance can amount up to 5% before the required analysis time starts to significantly increase, namely offer an interesting degree of freedom for the manufacturing process.

Considering the advancements in the field of

reactive ion etching (RIE), the recently comercialised Bosch process nowadays allows to etch structures consisting of an array of parallel slits with cross-sectional dimensions of say $d = 2$ μm by $w = 100$ μm, spaced apart by a distance of only $\delta = 2$ μm (cf. Fig. 3a), with a lateral resolution below 50 nm (corresponding to a σ_x of only 0.025), and with a depth ranging up to 100 μm, while still maintaining a side-wall slope of nearly exactly 90° [34]. At this point it should be remarked that the selection of the etch depth (which will determine the final segment block length) will have to be based on a compromise between the manageability of the segment blocks (fragility of the structures versus number of segments to be stacked) and the increased risk for sloped side-walls. Using one of the powerful modern replication methods [35], the etched structures can be used as a master mold to generate thousands and thousands of plastic replicas, which can then be used as dissolvable molds. By filling the slits of the mold with for example a sol–gel solution, the desired monolithic array structure (cf. Fig. 3) can be obtained.

More challenging aspects seem to be the mold dissolution and release process, the finishing of the entrance and outlet parts of the segments and the mechanical strength of the fabricated segment blocks. A final major hurdle will be the tedious and time consuming process of segment stacking. Such a process will certainly be much more expensive than the current column packing methods, but the effort will also partly be paid off by the increased packing uniformity (especially from column to column) which can be expected.

The above manufacturing scheme should not at all be regarded as the single possible method. Perhaps the present paper will stimulate others to come up with alternative solutions.

4.4. Future work

The obvious continuation of the present theoretical analysis is the consideration of other values of the channel and the stationary phase thickness, and to extend the range of investigated fluid velocities, in order to establish more accurate and more complete $\sigma^2_{t,junc}$ and ΔP_{junc} correlations. This will allow to explore the possibilities of the segmented column concept over a broader range of geometries and velocities.

With the established mathematical framework, allowing to cut the column into small representative elements and to link the results via the polydispersity theory of Schisla et al. [20], we can now attempt to repeat the current analysis for column geometries representing more closely the internal structure of the currently developed monolithic columns. With the insights gained from the present study, we are also well-armed to optimise the silicon etched 2D column structures for on-chip LC introduced a few years ago [36,37] and offering a very elegant way to obtain highly regular column packings. More specifically it will be possible to determine the optimal channel segment length as a function of the expected channel width variance of such structures (Fig. 13). Such a 2D etched column also seems to be the ideal intermediate step to experimentally verify the presently proposed calculations, because the practical elaboration of the full three-dimensional column concept seems to be a quite formidable task, and it is at present not very clear how this should best be attacked (see also Section 4.3).
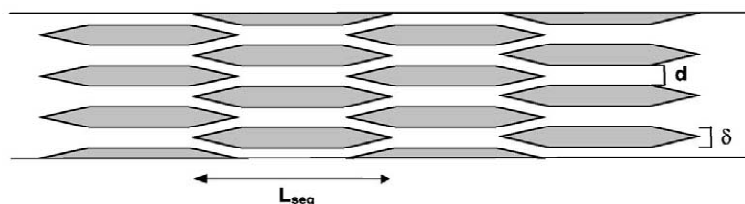

Fig. 13. Schematic top-view of a two-dimensional etched column offering the same degree of channel segment coupling as the three-dimensional column depicted in Fig. 2.

5. Conclusions

Building further on the work of Schisla et al. [20], and bringing in the results of a computational fluid dynamics simulation study, we have been able to confirm Schisla et al.'s [20] conjecture that the polydispersity effect ruining the separation efficiency of parallel bundle columns can be strongly alleviated by dividing the column into a large number of longitudinal segments, coupled in such a way that the mobile phase fluid is radially redistributed after each segment. Our calculations show that the coupling junction can be designed such that the advantage coming from the suppression of the polydispersity effect is much larger than the losses caused by the additional pressure-drop and band broadening. This is for example evidenced by the large gain in maximally achievable theoretical plate number which can potentially be obtained with the presently considered segmented parallel plate column.

For the considered column structure, the ideal segment length is found to vary between about 10 and 100 μm, depending on the degree of channel-to-channel thickness variance σ_x. When considering the minimal analysis time problem, it turns out that there is a relatively broad range of segment lengths (10 μm $< L_{\text{seg}} <$ 200 μm) wherein the analysis time is more or less independent of the segment length, at least for cases with $\sigma_x < 0.05$.

Although a number of important approximations and assumptions have been made, the fact that the presently considered (hypothetical) micro-structured monolithic column would allow to perform $N >$ 100 000 plate separations in a few hundred of seconds, i.e., about an order of magnitude faster than the best possible HPLC columns and also surpassing largely the currently developed monolithic LC columns, clearly points at the fact that the currently existing LC columns only yield a fraction of the full potential of the ideal, fully optimised LC column.

To achieve this absolute LC performance limit, columns are needed which are much better streamlined and have a much more regular internal structure than the present packed bed and monolithic columns. Radically new column manufacturing concepts will have to be developed to manufacture such columns. Whether it will ever be possible to ap- proach the absolute LC performance limit will hence depend largely upon the present and future advancements in the fields of micro-machining and micro-engineering.

6. Nomenclature

A, B, C, D	Constants defined by Eqs. (A.9)–(A.12) of Appendix A
A'', B'', C'', D''	Constants in H-expression given in Eq. (21)
A', B', C', D'	Constants in $\sigma_{\text{t,junc}}^2$-expression given in Eq. (14), see also Eqs. (A.9)–(A.12) of Appendix A
A'', B'', C'', D''	Constants in H-expression given in Eq. (21)
B_0	Column permeability, m^2
C	Tracer concentration, kg/m^3
d	Plate spacing = channel thickness, m
d_{f}	Stationary phase thickness = half of plate thickness δ, m
d_{m}	Mean channel thickness, m
D_{m}	Molecular diffusion coefficient mobile phase, m^2/s
D_{s}	Molecular diffusion coefficient stationary phase, m^2/s
E	Separation impedance factor (–)
H	Height equivalent to a theoretical plate, m
h	Reduced plate height, $h = H/d$, m
f_{F}	Friction factor
k	Retention factor (–)
K_1, K_2	Constants appearing in the pressure-drop correlations given in Eqs. (27) and (28) (–)
L	Column length, m
L_{seg}	Segment length, m
M_0, M_1, M_2	Respectively, zero- (s), first- (s^2) and second-order moment (s^3) of temporal tracer response at detector
N	Theoretical plate number (–)
$N_{1 \text{ m}}$	Maximal number of plates in 1 m column (–)
n_{s}	Number of segments in column (–)
R_{junc}	Flow resistance of coupling junction, see Eq. (23), kg/(m^2 s)

R_{seg}	Flow resistance of channel segment, see Eq. (23), kg/(m^2 s)
S_{junc}	Cross-sectional area of window at coupling plane, m^2
t_0	Residence time of mobile phase, s
t_R	Retention time, s
u_1	Velocity in individual channel, m/s
u_m	Velocity through channel with mean thickness, m/s
$\langle u \rangle$	Flow-rate averaged velocity of entire plate array, m/s
w	Channel width, m
x	Variable denoting relative difference between channel width of given channel and mean channel width: $x = (d - d_m)/d_m$, see Eq. (6) (–)
x, y, z	Cartesian coordinates, m

Greeks

α	Proportionality constant in Eq. (25) (–)
δ	Plate thickness, m
λ	Geometric factor in A-term of van Deemter equation, see Eq. (30) (–)
γ	Tortuosity in B-term of van Deemter equation, see Eq. (30) (–)
ΔP	Pressure drop, Pa
μ	Dynamic viscosity, kg/(m s)
ρ	Liquid density, kg/m^3
σ_d	Standard deviation of channel thickness distribution, see Eq. (6) (–)
σ_x	Relative standard deviation of channel thickness distribution, see Eq. (6) (–)
σ_t^2	Peak variance in the time domain, m^2
ψ	Flow resistance factor, $\psi = 12$ for a flat-rectangular channel (–)
Ω	Cross-sectional area of channel, m^2

Subscripts

1	Value referring to single channel
max	Maximal
seg	Segment
junc	Junction

Acknowledgements

Appendix A

Using $d = d_m(1 + x)$ and $u = u_m(1 + x)^2$ taken from Eqs. (6) and (8), and introducing the parameters A, B and C (see further: Eqs. (A.9) to (A.11)), Eq. (3) can, respectively, be written as:

$$t_R = \frac{L}{u_m} \cdot (1 + k) \cdot \frac{1}{(1 + x)^2} \tag{A.1}$$

$$\sigma_t^2 = A \cdot \frac{L}{u_m^3} \cdot \frac{1}{(1 + x)^6} + B \cdot \frac{L}{u_m} + C \cdot \frac{L}{u_m} \cdot \frac{1}{(1 + x)^2} \tag{A.2}$$

Using Eq. (1), the concentration integrals appearing in Eqs. (11) and (12) and representing the different order moments of the peaks in each individual channel can be calculated to yield:

$$\int_0^{+\infty} C_1(x,t) \cdot dt = C_0 t_R \tag{A.3}$$

$$\int_0^{+\infty} t C_1(x,t) \cdot dt = C_0 t_R^2 \tag{A.4}$$

$$\int_0^{+\infty} t^2 C_1(x,t) \cdot dt = C_0 \cdot (\sigma_t^2 + t_R^2) \cdot t_R \tag{A.5}$$

Using the approximation that:

$$(1 + x)^{n/m} = 1 - nx + \ldots \tag{A.6}$$

and limiting the series to the fourth or the sixth order term, and furthermore noting that:

$$\int_{-\infty}^{+\infty} f(x) \cdot dx = 1 \tag{A.7a}$$

$$\int_{-\infty}^{+\infty} x^2 f(x) \cdot dx = \sigma_x^2 \tag{A.7b}$$

$$\int_{-\infty}^{+\infty} x^4 f(x) \cdot dx = 3\sigma_x^4 \tag{A.7c}$$

while the integrals for the odd-order terms are identically zero, the integrals in the nominator and denominator of Eqs. (11) and (12) can now, respectively, be calculated as:

$$M_0 = w d_{\mathrm{m}} L C_0 \cdot (1 + k) \tag{A.8a}$$

$$M_1 = w d_{\mathrm{m}} \cdot \frac{L^2}{u_{\mathrm{m}}} \cdot C_0 \cdot (1 + k)^2 \cdot \left(1 + \sigma_x^2 + 3\sigma_x^4\right) \tag{A.8b}$$

$$M_2 = w d_{\mathrm{m}} L C_0 \cdot (1 + k)^2$$
$$\cdot \left[A \cdot \frac{L}{u_{\mathrm{m}}^3} \cdot \left(1 + 15\sigma_x^2 + 315\sigma_x^4 + \ldots \right) + B \right.$$
$$\cdot \frac{L}{u_{\mathrm{m}}} + C \cdot \frac{L}{u_{\mathrm{m}}} \cdot \left(1 + \sigma_x^2 + 3\sigma_x^4\right) + D \cdot \frac{L^2}{u_{\mathrm{m}}^2}$$
$$\left. \cdot \left(1 + 6\sigma_x^2 + 45\sigma_x^4 + \ldots \right) \right] \tag{A.8c}$$

with the D term originating from the t_{R}^2 term in Eq. (A.5).

Introducing now the expression given in Eqs. (A.8a)–(A.8c) into the expressions given in Eqs. (11) and (12), and defining A', B', C' and D' as:

$$A' = A \cdot \left(1 + 15\sigma_x^2 + 315\sigma_x^4 + \ldots\right) \quad \text{with}$$
$$A = 2D_{\mathrm{m}} \cdot (1 + k)^2 \tag{A.9}$$

$$B' = B \quad \text{with}$$
$$B = \frac{2}{210} \cdot \left(a + 9k + 25.5k^2\right) \cdot \frac{d_{\mathrm{m}}^2}{D_{\mathrm{m}}} \tag{A.10}$$

$$C' = C \cdot \left(1 + \sigma_x^2 + 3\sigma_x^4\right) \quad \text{with}$$
$$C = \frac{2}{3} \cdot k \cdot \frac{d_{\mathrm{f}}^2}{D_{\mathrm{s}}} \tag{A.11}$$

$$D' = D \cdot \left(4\sigma_x^2 + 40\sigma_x^4 + \ldots\right) \quad \text{with}$$
$$D = (1 + k)^2 \tag{A.12}$$

it is straightforward to obtain the expressions given in Eqs. (13) and (14).

References

[1] N. Tanaka, H. Kobayashi, K. Nakanishi, H. Minakuchi, N. en Ishizuka, Anal. Chem. 420 (2001) A429.
[2] J.E. Mac Nair, K.C. Lewis, J.W. Jorgenson, Anal. Chem. 69 (1997) 983.
[3] J.E. Mac Nair, K.D. Patel, J.W. Jorgenson, Anal. Chem. 71 (1999) 700.
[4] J.H. Knox, I. Grant, Chromatographia 24 (1987) 135.
[5] E.C. Peters, M. Petron, F. Svec, J.M. Frechet, Anal. Chem. 70 (1998) 2296.
[6] R.T. Kennedy, I. German, J.E. Thompson, S.R. Witowski, Chem. Rev. 99 (1999) 3081.
[7] K. Walhagen, K.K. Unger, M.T.W. Hearn, J. Chromatogr. A 887 (2000) 165.
[8] K.K. Unger, M. Huber, T.P. Hennessy, M.T.W. Hearn, K. Walhagen, Anal. Chem. 74 (2002) 200A.
[9] W. Kok, Chromatographia 51 (Suppl.) (2000) S28.
[10] I. Gusev, X. Huang, C. Horvath, J. Chromatogr. A 855 (1999) 273.
[11] R. Hahn, A. Jungbauer, Anal. Chem. 72 (2000) 4853.
[12] H. Minakuchi, N. Ishizuka, K. Nakanishi, N. Soga, N. Tanaka, J. Chromatogr. A 828 (1998) 833.
[13] N. Ishizuka, H. Minakuchi, K. Nakanishi, N. Soga, H. Nagayama, K. Hosoya, N. Tanaka, Anal. Chem. 72 (2000) 1275.
[14] B. Bidlingmaier, K.K. Unger, N. von Doehren, J. Chromatogr. A 832 (1999) 11.
[15] J.H. Knox, J. Chromatogr. Sci. 7 (1980) 453.
[16] H. Poppe, J. Chromatogr. A 778 (1997) 3.
[17] Y. Guo, L.A. Colon, Chromatographia 43 (1996) 135.
[18] R. Swart, S. Brouwer, J.C. Kraak, H. Poppe, J. Chromatogr. A 732 (1996) 201.
[19] H. Ding, Ph.D. Thesis, University of Minnesota, MN, 1992.
[20] D.K. Schisla, H. Ding, P.W. Carr, E.L. Cussler, AIChE J. 39 (1993) 946.
[21] C.K. Harris, D. Roekaerts, F.J.J. Rosendahl, H. Wang, Chem. Eng. Sci. 51 (1996) 1569.
[22] J.A.M. Kuipers, W.P.M. van Swaaij, Rev. Chem. Eng. 13 (1997) 1.
[23] A. Cifuentes, H. Poppe, Chromatographia 255 (1994) 391.
[24] M. Martin, J.-L. Jurado-Baizaval, G. Guiochon, Chromatographia 16 (1982) 98.
[25] P.P.H. Tock, P.P.E. Duijsters, J.C. Kraak, H. Poppe, J. Chromatogr. 506 (1990) 185.
[26] D. Dutta, D.T. Leighton Jr., Anal. Chem. 73 (2001) 504.
[27] M.R. Doshi, P.M. Daiya, W.N. Gill, Chem. Eng. Sci. 33 (1978) 795.
[28] H. Schlichting, Boundary-Layer Theory, McGraw Hill, London, 1958.
[29] H. Poppe, Anal. Mag. 22 (1994) 22.
[30] J.O. Wilkes, Fluid Mechanics for Chemical Engineers, Prentice Hall, London, 1999.
[31] E.D. Katz, K. Ogan, R.P.W. Scott, in: F. Bruner (Ed.), The Science of Chromatography—Lectures Presented at the A.J.P. Martin Honorary Symposium, Urbino, 27–31 May, 1985, Journal of Chromatography Library, Vol. 32, Elsevier, Amsterdam, 1985, p. 403.

[32] P. Bristow, J.H. Knox, Chromatographia 10 (1977) 279.

[33] J.H. Knox, J. Chromatogr. A 831 (1999) 3.

[34] A. Rickard, M. McNie, presented at the SPIE International Conference on Microelectronic and MEMS Technologies, Edinburgh, May 2001.

[35] E. Kim, Y. Xia, G.M. Whitesides, Nature 376 (1995) 581.

[36] B. He, N. Tait, F.E. Regnier, Anal. Chem. 70 (1998) 3790.

[37] F.E. Regnier, J. High Resolut. Chromatogr. 23 (2000) 19.